

SIMBA Simulation: The Effect of Feedback Physics on Matter Distribution in the Cosmic Web

Chenze Dong,^{1,2}★ Florian Dedieu,³† Daniela Galárraga-Espinosa,² Khee-Gan Lee,^{1,2} Daniele Sorini,⁴ Romeel Davé^{5,6}

¹Center for Data-Driven Discovery, Kavli IPMU (WPI), UTIAS, The University of Tokyo, Kashiwa, Chiba 277-8583, Japan

²Kavli Institute for the Physics and Mathematics of the Universe, The University of Tokyo, 5-1-5 Kashiwanoha, Kashiwa, Chiba, 277-8583, Japan

³ENS Paris-Saclay, Paris-Saclay University, 4 Av. des Sciences, 91190 Gif-sur-Yvette, France

⁴Institute for Computational Cosmology, Department of Physics, Durham University, South Road, Durham, DH1 3LE, United Kingdom

⁵Institute for Astronomy, University of Edinburgh, Royal Observatory, Edinburgh EH9 3HJ, UK

⁶Department of Physics and Astronomy, University of the Western Cape, Bellville, Cape Town 7535, South Africa

Accepted XXX. Received YYY; in original form ZZZ

ABSTRACT

The discrepancy between the early-time estimation and late-time observation on the cosmic baryon content — the ‘missing baryon problem’ - is a longstanding problem in cosmology. Although recent studies with fast radio bursts (FRBs) have largely addressed this discrepancy, the precise spatial distribution of these baryons remains uncertain due to the effect of galaxy feedback. Cosmological hydrodynamical simulations such as SIMBA have shown that the partitioning of baryons between the intergalactic medium (IGM) and haloes is sensitive to feedback models, motivating the connection of baryon distribution with feedback physics. With the SIMBA simulation suite, this study investigates how feedback affects the distribution of matter within large-scale cosmic structures, with implications for FRB foreground modeling. We apply the T-web method to classify the cosmic web into different structures: knots, filaments, sheets, and voids. We then analyze how the different feedback variants of SIMBA affect the distribution of matter within each structure. Our results show that in SIMBA, the fractions of IGM gas in different cosmic web structures vary only a few percent under different feedback models. However, jet feedback produces noticeable changes in the gas distribution within structures, enhancing the diffuse IGM on the outskirts of filaments and knots. This research provides a new perspective on the impact of feedback on the IGM and motivates a refined data model for the FRB foreground mapping.

Key words: intergalactic medium – methods: numerical – large-scale structure of Universe – fast radio bursts

1 INTRODUCTION

The “missing baryon problem” describes the observational deficit of the cosmic baryon density parameter, Ω_b , observed in the low-redshift universe when compared to early-time measurements from cosmic microwave background (CMB) studies (e.g., Planck Collaboration et al. 2016, 2020) as well as Big Bang Nucleosynthesis constraints from light element abundances (Steigman 2010; Cooke 2024). Fukugita et al. (1998) noted that a mere 10% of the universe’s baryonic matter is found in galaxies as stars or interstellar medium (ISM) gas, with the majority existing in a state of diffuse, ionized intergalactic medium well outside of observed galaxies.

This issue was extensively studied in both theory and observations in the 2000s, as exemplified in the works by, e.g., Fukugita & Peebles (2004); Cen & Ostriker (2006); Bregman (2007). The pioneering simulation study conducted by Cen & Ostriker (1999) identified the warm-hot intergalactic medium (WHIM) as a potential reservoir for the elusive baryons. Detecting the WHIM presents a significant challenge since it is not sufficiently hot to significantly emit X-rays and not sufficiently cool to allow for radio emissions. Subsequent

works (e.g., Kang et al. 2005; Davé et al. 2001; Kravtsov et al. 2002; Kang et al. 2007; Tornatore et al. 2010; Hong et al. 2014) revealed that the production of such WHIM was related to so-called “baryonic effects”, especially gas shock heating from gravitational collapse, and galactic feedback.

Simultaneously, various observational efforts are undertaken to locate the missing baryons. Guided by predictions from simulations (Cen et al. 2001; Yoshikawa et al. 2003; Cen & Fang 2006; Hallman et al. 2007; Davé et al. 2010; Oppenheimer et al. 2012), Lyman- α absorption and O VI absorption have been utilized in attempts to detect the presence of the WHIM (Fang et al. 2002; Bregman 2007; Prochaska et al. 2017; Stocke et al. 2013; Nicastro et al. 2018; Kovács et al. 2019), alongside using the Sunyaev-Zel’dovich (SZ) effect (Shao et al. 2011; Ferraro et al. 2016; Chiu et al. 2018; de Graaff et al. 2019). Despite these comprehensive observation efforts, by 2019, 20% of baryons remained undetected.

The advent of fast radio bursts (FRBs; see reviews Cordes & Chatteerjee 2019; Glowacki & Lee 2024) as extragalactic probes has significantly altered the situation. FRBs are radio pulses lasting milliseconds, originating from extragalactic sources with unknown mechanisms (see Platts et al. 2019 for a living catalog of FRB theories).

★ E-mail: dong-chenze@g.ecc.u-tokyo.ac.jp

† E-mail: florian.dedieu@ens-paris-saclay.fr

The dispersion measure (DM) of an FRB,

$$DM = \int n_e \frac{ds}{1+z}, \quad (1)$$

quantifies its frequency-dependent time delay, determined by the integration of the electron density n_e along the line-of-sight path element ds . Given that $\approx 99\%$ of extragalactic baryons are ionized after cosmic reionisation (e.g., [Neeleman et al. 2016](#)), the DM is effectively a volume-weighted probe of cosmic baryons, in contrast with most other probes of the cosmic baryons which are halo-centric. By analyzing 7 FRBs with host galaxy identification ('localised') detected by ASKAP, [Macquart et al. \(2020\)](#) reported that the redshift-DM relationship of these FRBs was in good agreement with standard Λ CDM cosmology. This result has technically 'detected' the missing baryons but still does not address the question of where they reside, as the FRB DM measures the integrated electron density along the line-of-sight. Then the relative distribution of cosmic baryons in different parts of the Universe, connected to the scatter of the redshift-DM relation of FRBs, remains unclear.

In modern cosmological hydrodynamical simulations (e.g., [Schaye et al. 2010](#); [Vogelsberger et al. 2014](#); [Hopkins et al. 2014](#); [Bryan et al. 2014](#); [Schaye et al. 2015](#); [McCarthy et al. 2017](#); [Pillepich et al. 2018](#); [Davé et al. 2019](#)), galaxy 'feedback processes' such as energy injection from stellar winds, supernova explosions, and AGN-driven outflows are introduced primarily to regulate the excessive star formation. Feedback has been found to have a substantial impact on the overall distribution of baryonic gas, especially in the WHIM ([Haider et al. 2016](#); [Martizzi et al. 2019](#)). Furthermore, different feedback models predict different partitions of baryons within, around, and beyond galactic haloes ([Heckman & Thompson 2017](#); [Davies et al. 2019](#); [Tollet et al. 2019](#); [Christiansen et al. 2020](#); [Davies et al. 2020](#); [Lim et al. 2021](#); [Sorini et al. 2022](#); [Ayromlou et al. 2023](#); [Angelinelli et al. 2023](#); [Appleby et al. 2023](#); [Sorini et al. 2024](#)) and across distinct cosmic web environments (e.g. [Martizzi et al. 2019](#); [Bradley et al. 2022](#)). Thus, measuring the mass fraction of baryons across different scales and environments represents a potentially interesting method for constraining the physics underlying feedback processes.

Although the baryon distribution imprinted in the FRB DM is a promising probe of feedback, the relatively low number of localised FRBs limited the application of this approach. Even with many efforts to detect FRBs by Canadian Hydrogen Intensity Mapping Experiment (CHIME; [CHIME/FRB Collaboration et al. 2021](#)), Commensal Real-Time ASKAP Fast Transient (CRAFT; [Macquart et al. 2010](#)), MeerKAT TRAnsients and Pulsars (MeerTRAP; [Sanidas et al. 2018](#)), and Deep Synoptic Array (DSA; [Kocz et al. 2019](#)), the localised FRBs to date are far from enough ($\sim 10^3$ are needed according to [Batten et al. 2022](#)) to constrain feedback models. However, [Lee et al. \(2022\)](#) argued that combining FRBs dispersion measures with spectroscopic observations of foreground galaxies ("FRB foreground mapping") enhances the precision of joint constraints on the intergalactic medium and circumgalactic medium (CGM) baryon distributions beyond that of localised FRBs alone. An early attempt by [Simha et al. \(2020\)](#) involved decomposing DM observed from a single FRB into contributions from the Milky Way, the extragalactic cosmic baryons, and the host galaxy. This idea was further extended in the FRB foreground mapping survey, FLIMFLAM, ([Lee et al. 2022](#); [Khrykin et al. 2024b](#); [Huang et al. 2024](#)), where the decomposition adopted was

$$DM = DM_{MW} + DM_{haloes} + DM_{IGM} + DM_{host} \quad (2)$$

where DM_{MW} and DM_{host} are the contributions from the Milky Way and the FRB host, respectively. The remaining contribution, called

'cosmic baryon contribution', is thus separated into DM_{haloes} (circumgalactic medium, CGM, in intervening haloes) and DM_{IGM} (intergalactic medium). The foreground galaxy observations enable one to find the haloes along the FRB line of sight ("intervening haloes") and also to reconstruct the large-scale density field ρ_m using galaxies as biased tracers (e.g. the ARGO code used in FLIMFLAM [Ata et al. 2015, 2017](#)). Then DM_{haloes} is calculated with the intervening haloes assuming a radial profile (see [Khrykin et al. 2024a](#) for more discussion), while DM_{IGM} is calculated following Equation 3 (using Equation 1):

$$DM_{IGM} = \int n_{e,IGM} \frac{ds}{1+z} \approx \int \bar{n}_{e,IGM} (1 + \delta_m) \frac{ds}{1+z} \quad (3)$$

where $\delta_m(\mathbf{x}) = \rho_m(x)/\bar{\rho}_m - 1$ is the mass overdensity, and $\bar{n}_{e,IGM}$ is the mean electron number density in the IGM, defined in the following Equation 4.

$$\bar{n}_{e,IGM} = f_{IGM} \frac{X_H m_{He} + 2Y_{He} m_H}{m_H m_{He}} \Omega_b \rho_c(z) \quad (4)$$

In this model, f_{IGM} is the fraction of baryons residing in the IGM, a free parameter to be determined in FLIMFLAM's analysis. Also, in Equation 3, the default assumption is that the baryon-to-total-mass fraction is the cosmic value ($\rho_{gas,IGM} = (1 + \delta_m)\bar{\rho}_{gas,IGM}$) and the IGM gas is fully ionized ($n_{e,gas,IGM} \propto \rho_{gas,IGM}$).

In a comparative study of several feedback variants of the SIMBA cosmological hydrodynamical simulation, [Khrykin et al. \(2024a\)](#) found that the overall balance of cosmic baryons between the halo CGM and large-scale diffuse IGM is significantly altered by the feedback model adopted. In particular, they found that feedback from long-range AGN jets may increase the IGM gas fraction by approximately 20% and decrease the CGM baryon fraction by around 50% relative to weaker feedback models. Their results motivate the parametrization of $DM_{cosmic} = DM_{IGM} + DM_{haloes}$ in FLIMFLAM as a probe of feedback, although [Hussaini et al. \(2025\)](#) recently claimed evidence of feedback from lower limits on f_{igm} in low-DM localised FRBs from the DSA survey.

In this study, we follow up on [Khrykin et al. \(2024a\)](#) to explore whether different feedback models might redistribute cosmic baryons across the different parts of the cosmic web. Specifically, we employ the T-web method to classify the cosmic web (e.g., [Hahn et al. 2007](#); [Forero-Romero et al. 2009](#); [Cautun et al. 2014](#)) in the SIMBA simulations into 'voids', 'sheets', 'filaments', and 'knots', based on the local dynamics of the density field collapse. Subsequently, we will evaluate if the fraction of IGM within the filaments is affected by the feedback model, similar to jet impact on IGM/CGM distribution as reported by [Khrykin et al. \(2024a\)](#). We consider the decomposition of DM as

$$\begin{aligned} DM_{IGM} &= DM_{voids} + DM_{sheets} + DM_{filaments} + DM_{knots} \\ &= \sum_j \int_j f_{IGM,j} (1 + \delta_m) A(z) \frac{ds}{1+z} \\ &= \sum_j f_{IGM,j} \int_j (1 + \delta_m) A(z) \frac{ds}{1+z} \end{aligned} \quad (5)$$

Where $f_{IGM,j} = \frac{M_{IGM}}{M_{baryon}}|_j$, $j \in \{\text{voids, sheets, filaments, knots}\}$ is the fraction of baryons in the IGM for the different cosmic web environments, while $A(z) = \frac{X_H m_{He} + 2Y_{He} m_H}{m_H m_{He}} \Omega_b \rho_c(z)$. As it is already revealed by [Khrykin et al. \(2024a\)](#) that the different feedback models

will be reflected in the global f_{IGM} value, we will rewrite $f_{\text{IGM},j}$ as

$$\begin{aligned} f_{\text{IGM},j} &= \frac{M_{\text{all,IGM}}}{M_{\text{all,baryon}}} \frac{M_{\text{all,baryon}}}{M_{j,\text{baryon}}} \frac{M_{j,\text{IGM}}}{M_{\text{all,IGM}}} \\ &= f_{\text{IGM}} \frac{F_{j,\text{IGM}}}{F_{j,\text{baryon}}}, \end{aligned} \quad (6)$$

where $F_{j,\text{IGM}} = \frac{M_{j,\text{IGM}}}{M_{\text{all,IGM}}}$ and $F_{j,\text{baryon}} = \frac{M_{j,\text{baryon}}}{M_{\text{all,baryon}}}$ are the partitions of IGM gas and baryons in each type of structure, respectively. The potential improvement of the model that incorporates cosmic web structures would stem from the variation in their ratio $F_{j,\text{IGM}}/F_{j,\text{baryon}}$ among the feedback models. In this paper, we investigate whether this refined model significantly improves the inference power of FRB observations towards feedback.

The paper is structured as follows: in Section 2, we present the SIMBA simulation utilized in this study and introduce the T-web method on cosmic web classification. In Section 3, we then demonstrate our classification applied to the SIMBA suites. We compare the partition of matter in different IGM environments in Section 4 to verify the improvement on the refined model (Equation 5 and 6). Then, we examine the correlation between overdensity and gas density in Section 5. In Section 6, we discuss the results and implications for future observation. Finally, we summarize our main findings in Section 7. We assume the Planck15 cosmology (Planck Collaboration et al. 2016) ($\Omega_m = 0.3$, $\Omega_\Lambda = 1 - \Omega_m = 0.7$, $\Omega_b = 0.048$, $h = 0.68$, $\sigma_8 = 0.82$, $n_s = 0.97$) to stay consistent with the SIMBA simulation. Finally, throughout this paper, we restrict our analysis to $z = 0$ and leave the exploration on higher redshifts in future works.

2 DATA AND METHODS

In this section, we give a brief introduction to the simulation data used in Section 2.1, and the method of defining the cosmic structures in Section 2.2. We also show how we map the particle-based simulation data into the density fields in Section 2.3.

2.1 The SIMBA simulation

In this study, we adopted the SIMBA simulation¹ (Davé et al. 2019) for our cosmic web analysis. SIMBA is a modern suite of galaxy formation simulations, successor of the Mufasa simulation (Davé et al. 2016), and which aims to reproduce the physics of the universe at diverse spatial scales in a full cosmological context. In the following section, we introduce the specifications of SIMBA and its feedback variants.

2.1.1 Cosmology and Numerical Scheme

SIMBA adopts a Λ CDM cosmology following the Planck15 measurements (Planck Collaboration et al. 2016). The simulation is then performed with the massively-parallel gravito-hydrodynamic code GIZMO, in its Meshless Finite Mass (MFM) version. Gas elements and dark matter (DM) are simulated together, the latter being represented through a set of collisionless Lagrangian particles solved via a tree-particle-mesh algorithm, and shocks are computed via a Riemann solver without the need for artificial viscosity.

¹ <http://Simba.roe.ac.uk/>

2.1.2 Gas Physics and Star Formation

In SIMBA, the Grackle-3.1 library (Smith et al. 2016) handles all the cooling and heating processes (mainly radiation and photo-ionization), which take into account metal cooling and the non-equilibrium evolution of the primordial elements. The ionization background is taken from Haardt & Madau (2012), modified in order to take into account the self-shielding effect in a self-consistent way, following the prescription of Rahmati et al. (2013).

Star formation is modeled with a Schmidt (1959) law for H_2 , which is assessed on the basis of the subgrid model of Krumholz & Gnedin (2011), modified to take into account variations in numerical evolution (Davé et al. 2016). Star formation rate (SFR) is evaluated from the H_2 density and the dynamical time only (Davé et al. 2019; Kennicutt 1998). Metal enrichment takes into consideration 11 elements (H, He, C, N, O, Ne, Mg, Si, S, Ca, Fe) then, as enrichment processes, Type Ia supernovae (IaSNe) (Iwamoto et al. 1999), Type II supernovae (IISNe) (Nomoto et al. 2006), and Asymptotic Giant Branch (AGB) stars (Oppenheimer & Davé 2006), as well as the fact that a part of the metal can be contained in dust.

2.1.3 Stellar and SMBH Feedback

The model of star formation-driven winds used by SIMBA involves decoupled metal-enriched kinetic winds whereby 30% of the winds particles are ejected in a hot phase, with temperatures determined by the difference between the supernovae energy and the winds kinetic energy, while the others are ejected with a temperature of around 10^3 K. The mass loading factor and the winds velocity are the main free parameters, chosen in this simulation to be in agreement with the FIRE zoom-in simulations (Muratov et al. 2015; Anglés-Alcázar et al. 2017). See Davé et al. (2019) for the complete details. The outflows are enriched in metals, accounting for the impact of the IISNe that extricate heavy elements from the ISM. Once ejected, wind particles cannot radiate and are compelled to thermally transfer their energy to the CGM.

SIMBA also implements supermassive black hole (SMBH) growth and SMBH feedback. SMBH growth is modeled differently depending on the physical state of the accreted gas. The ISM gas within the SMBH kernel, always cold in this simulation ($T \leq 10^5$ K), follows a torque-limited accretion mode, taken from Hopkins & Quataert (2011), which is physically related to gravitational instabilities of cold gaseous disks which drive mass inflows. The non-ISM hot gas ($T \geq 10^5$ K) usually has a more spherical distribution, which explains the choice of a Bondi accretion rate, given by the standard Bondi (1952) formula shown in Equation 7.

$$\dot{M}_{\text{Bondi}} = \epsilon_m \frac{4\pi G^2 M_{\text{SMBH}}^2 \rho}{(v^2 + c_s^2)^{3/2}} \quad (7)$$

where ρ is the mean density of the hot gas calculated within the SMBH kernel, c_s is its average sound velocity, and v is its average velocity relative to the center of the SMBH. ϵ_m is an attenuation factor set such as $\epsilon_m = 0.1$ to make the Bondi accretion rate consistent with the previous torque-limited accretion mode (Davé et al. 2019).

In SIMBA, there are three implementations of AGN feedback, designed to be consistent with the observed dichotomy in real AGN feedback (see e.g Heckman & Best 2014) that usually involves a radiative mode at high accretion rates, and a jet mode for slow-accreting AGN. First, the fast-accreting AGN can emit what are called *Radiative AGN winds*. This “high-accretion feedback mode” is adopted when the SMBH has an Eddington ratio $f_{\text{ED}} = \dot{M}/\dot{M}_{\text{ED}} \geq 0.2$, and

consists in ejecting gas particles from the vicinity of the SMBH along a direction parallel to the total angular momentum of the accretion disk (typically the 256 closest gas particles to the BH). The resulting bipolar outflows velocity depends only on the SMBH mass and follows Equation 8, based on the analysis of the X-rays emission of ionized gas stem from $z < 0.8$ SDSS AGN (Perna et al. 2017a).

$$v_{\text{RW}} = 500 + \frac{500}{3} \left(\log \left(\frac{M_{\text{BH}}}{M_{\odot}} \right) - 6 \right) \text{ km/s} \quad (8)$$

Ejection of the particles is adiabatic, and their temperature is consistent with that of the electrons observed in actual ionized gas outflows, with an order of magnitude of 10^4 K (Perna et al. 2017b).

The “slow-accreting mode” is activated when $f_{\text{ED}} \leq 0.2$. It involves the same bipolar mass-loaded ionized gas ejections as for the high accretion mode, but with an outflows velocity additionally depending on f_{ED} . This new dependence, denoted by the equation 9, allows to reach dramatic outflow velocities when the Eddington ratio decreases, with an order of magnitude as high as 10^4 km/s. However, the velocity boost is capped at 7000 km/s, that generally corresponds to $f_{\text{ED}} \lesssim 0.02$.

$$v_{\text{jets}} = v_{\text{RW}} + 7000 \log \left(\frac{0.2}{f_{\text{ED}}} \right) \text{ km/s} \quad (9)$$

In addition to a low Eddington ratio, the jets mode requires the condition $M_{\text{BH}} > M_{\text{BH,lim}}$, with $M_{\text{BH,lim}} = 10^{7.5} M_{\odot}$, which aims to prevent AGN with low masses to emit jets when they temporarily accrete little gas, as observed (Barišić et al. 2017).

In both cases, as gas particles are ejected in the same direction and from their personal positions, radiative winds and jets outflows are bipolar, with an opening angle assumed to be null and a finite cross section extent generally $\lesssim 1$ kpc. On one hand, this choice makes sense for the low accretion mode, as AGN jets are actually observed as thin collimated ejections. As for radiative AGN winds, this model may be a bit reductive as the opening angle is likely to be greater. Nevertheless, Davé et al. (2019) justifies it by saying that, even if they were, for instance, spherical, they would probably get collimated on scales that cannot be resolved in SIMBA.

Finally, fast-accreting SMBH with fully boosted jets can exert X-ray heating feedback if the galaxy is poor in gas, with a gas mass fraction $f_{\text{m,gas}} = M_{\text{tot}}/M_* < 0.2$. This definition is motivated by the observed inclination of the slow radiative winds to appear in more gaseous galaxies, where there would be important radiative losses (Best & Heckman 2012). The X-ray heating is applied to the gas particles within the SMBH accretion kernel, computed following Equation 12 of Choi et al. (2012), scaling on the inverse of the square of their distance from the SMBH. The energy conversion is made depending on whether the gas belongs to the ISM or not. The cold ISM gas is simply heated and its temperature is increased depending on the heating flux at its position. Half of the heating energy given to the non-ISM gas is converted into kinetic energy, in the form of a radial outwards kick, while the rest is kept as thermal energy. The X-ray heating feedback has little effect on the galaxy mass function, but plays a critical role for galaxy quenching.

2.1.4 SIMBA feedback variants

The SIMBA simulation suites contain one flagship run with a volume of $(100 \text{ cMpc/h})^3$ and full feedback physics, and many other variant runs with modifications on volume and physics included. To study the properties of the cosmic web affected by different feedback mechanisms, we utilized several $(50 \text{ cMpc/h})^3$ feedback variants of SIMBA

in this research (see Table 1). It should be noted that all the SIMBA feedback variants begin with identical initial conditions (IC), facilitating the field-level comparison among the runs. We also adopted the Caesar² halo catalogs provided in SIMBA data repository. Most post-processing work on simulation snapshots is done with the light-weighted analysis package for Gadget output, pygad (Röttgers et al. 2020).

2.2 Classifying the cosmic web

In this work, we derive the cosmic web classification based on the T-web methodology. The latter relies on the three eigenvalues $\lambda_1 \geq \lambda_2 \geq \lambda_3$ of the deformation tensor ψ_{ij} , where ψ_{ij} is the Hessian matrix of the rescaled gravitational potential $\tilde{\phi} = \phi/4\pi G\bar{\rho}$, which also follows Poisson’s Equation:

$$\begin{cases} \Delta \tilde{\phi}(\mathbf{x}) = \delta(\mathbf{x}) \\ \psi_{ij}(\mathbf{x}) = \frac{\partial^2 \tilde{\phi}}{\partial x_i \partial x_j}(\mathbf{x}) \end{cases} \quad (10)$$

where $\delta(\mathbf{x})$ is the overdensity, defined in section 1. To mitigate numerical artifacts on small scales, we applied a Gaussian smoothing kernel to the density field before the subsequent calculation. The smoothing scale R_{sm} is also a hyperparameter of the T-web method and defines the scale of features to be extracted in the cosmic web analysis. We choose $R_{\text{sm}} = 2 \text{ Mpc/h}$, which we will justify later on.

After the density smoothing step, we calculate the deformation tensor through Fast Fourier Transform (FFT) and then obtain the classification depending on the number of eigenvalues larger than a certain threshold λ_{th} , another hyperparameter in the method.

$$\text{Classification} = \begin{cases} \text{Node,} & \lambda_1 \geq \lambda_2 \geq \lambda_3 \geq \lambda_{\text{th}} \\ \text{Filament,} & \lambda_1 \geq \lambda_2 \geq \lambda_{\text{th}} \geq \lambda_3 \\ \text{Sheet,} & \lambda_1 \geq \lambda_{\text{th}} \geq \lambda_2 \geq \lambda_3 \\ \text{Void,} & \lambda_{\text{th}} \geq \lambda_1 \geq \lambda_2 \geq \lambda_3 \end{cases} \quad (11)$$

According to Hahn et al. (2007), λ_{th} was set as zero based on the Zel’dovich approximation. However, Forero-Romero et al. (2009) indicated that such a choice is inadequate for filtering structures with large collapsing timescales (i.e., positive but small λ_{th}).

In this study, we selected $(\lambda_{\text{th}}, R_{\text{sm}}) = (0.16, 2 \text{ h}^{-1} \text{ cMpc})$ after careful assessment of different combinations of hyperparameters (see Appendix B). We start by choosing a smoothing length of 2 cMpc/h, which is motivated by the spatial resolution of the density field reconstruction in FLIMFLAM (1.875 cMpc/h). This smoothing scale is at the limit of the best resolution that can be achieved when reconstructing density fields using galaxy surveys, which is due to limitations on the observations and density field modeling (Khrykin et al. 2024b).

For the choice of the eigenvalue threshold, we use $\lambda_{\text{th}} = 0.16$ as the choice effectively restores the visual representation of smoothed cosmic web structures. At the same time, it aligns the mass and volume fractions of our cosmic web classification with the Martizzi et al. (2019) to 2% level.

A concise description of our classification workflow is given below.

- (i) Starting with simulation snapshots, we first run a cloud-in-cell (CiC) algorithm to obtain the matter density field $\rho_m(\mathbf{x})$. The algorithm will loop over all types of simulations particles, and

² <https://caesar.readthedocs.io/en/latest/>

Simulation	Box size (cMpc/h)	N_p	$m_{DM}(10^7 M_\odot)$	$m_{gas}(10^7 M_\odot)$	Stellar	AGN winds	AGN jets	AGN X-ray
Feedback variants								
SIMBA-50	50	2×512^3	9.6	1.82	Y	Y	Y	Y
SIMBA-nox	50	2×512^3	9.6	1.82	Y	Y	Y	N
SIMBA-nojet	50	2×512^3	9.6	1.82	Y	Y	N	N
SIMBA-noagn	50	2×512^3	9.6	1.82	Y	N	N	N
SIMBA-nofb	50	2×512^3	9.6	1.82	N	N	N	N

Table 1: Specification of SIMBA runs used in this study. All the feedback variants have the same box size and mass resolution, but with different feedback mechanism turning off. N_p is total number of dark matter particles and gas cells. The m_{DM} and m_{gas} are the mass resolution for dark matter particles and gas cells, respectively. Each feedback variant run of SIMBA contains 512^3 dark matter particles and the same number of gas particles. The detail of feedback implementation is introduced in Section 2.1.

distribute the mass of the particles onto a grid representing the simulation volume. We further calculate the overdensity field $\delta(\mathbf{x})$ and subsequently smooth $\delta(\mathbf{x})$ with a Gaussian kernel with $R_{sm} = 2 h^{-1} \text{cMpc}$.

- (ii) The deformation tensor is given by equation 10; here we switched to the Fourier (\mathbf{k}) space to perform the computation. One can calculate the deformation tensor in Fourier space by

$$\psi_{ij}(\mathbf{k}) = -k_i k_j \phi(\mathbf{k}) = \frac{k_i k_j}{\|\mathbf{k}\|^2} \delta(\mathbf{k}) \quad (12)$$

Therefore we obtain the \mathbf{k} -space overdensity $\delta(\mathbf{k})$ via the Fast Fourier Transform (FFT), then derive the \mathbf{k} -space deformation tensor $\psi_{ij}(\mathbf{k})$ using Equation 12. Finally, we perform inverse FFT on $\psi_{ij}(\mathbf{k})$ to get $\psi_{ij}(\mathbf{x})$.

- (iii) For the deformation tensor associated with each voxel, we calculate its eigenvalues $\lambda_1, \lambda_2, \lambda_3$, and get the T-web classification from the criteria 11 adopting $\lambda_{th} = 0.16$.

2.3 Describing the matter distribution

This study aims primarily to explore the potential of constraining feedback models from the distribution of gas within the cosmic web using Fast Radio Bursts (FRBs). The principal methodology involves the volumetric classification detailed in Section 2.2. We analyze the spatial distributions of several related quantities: total matter (dark matter and baryons), baryonic gas, and free electrons. Of these quantities, the total matter defines the cosmic web, baryonic gas serves as the direct recipient of feedback effects, and electron density represents the most direct observable within FRB measurements.

The electron number $N_{e,\text{cell}}$ of each gas cell is calculated with the mass of the gas cell M_{gas} , the hydrogen abundance X_H , and the electron abundance η_e :

$$N_{e,\text{cell}} = \eta_e \frac{X_H M_{\text{gas}}}{m_p} \quad (13)$$

We generate the grid of matter density ρ_m , baryon density ρ_b , and electron number N_e by running the CiC algorithm over simulation particles (dark matter, stars, and black holes) and cells (gas) in the $z = 0$ snapshot of SIMBA. We denote the densities of matter, gas, and free electrons as ρ_m, ρ_g and ρ_e . The normalized overdensities are $\delta_m = \rho_m / \bar{\rho}_m - 1$, $\delta_g = \rho_g / \bar{\rho}_g - 1$ and $\delta_e = \rho_e / \bar{\rho}_e - 1$, respectively.

Combining the density grids and the cosmic web classification, it is straightforward to calculate the mass fractions:

$$F_j^i = \frac{M_j^i}{\sum_j M_j^i} \quad (14)$$

where the index $i \in \{\text{SIMBA-50, SIMBA-nox, SIMBA-nojet, SIMBA-noagn, SIMBA-nofb}\}$, $j \in \{\text{voids, sheets, filaments, knots}\}$.

Unlike dark matter, the quantities of baryon, gas, and free electrons are subject to change across different feedback scenarios, as feedback mechanisms influence star formation and black hole accretion, leading to variations in baryonic matter remaining as a diffuse medium. To remove variations in total amounts, we compute the fraction using the subsequent normalization:

$$\begin{aligned} F_{j,\text{baryon}}^i &= \frac{M_{j,\text{baryon}}^i}{\sum_j M_{j,\text{baryon}}^i}, \\ F_{j,\text{IGM}}^i &= \frac{M_{j,\text{IGM}}^i}{\sum_j M_{j,\text{IGM}}^i}, \\ F_{j,e}^i &= \frac{N_{j,e}^i}{\sum_j N_{j,e}^i}. \end{aligned} \quad (15)$$

The gridded density field also allows us to define a ‘local’ gas fraction f_{gas}

$$f_{\text{gas}} = \frac{\rho_{\text{gas}}}{f_b \rho_{\text{tot}}}, \quad (16)$$

where $f_b = \Omega_b / \Omega_m$ is the cosmic baryon fraction and ρ_{gas} is the density value of a given grid voxel. Thereby, $f_{\text{gas}} > 1$ corresponds to a gas excess with respect to the average cosmic gas fraction, while $f_{\text{gas}} < 1$ corresponds to a gas deficit. The definition is inspired by Khrykin et al. (2024a), where a similar quantity is used to describe the gas content inside the galaxy haloes. To suppress the numerical artifacts but avoid losing the structure of interest when we compute the local gas fraction, we apply a minimal Gaussian smoothing $r_{\text{smoothing}} = 0.1 \text{ cMpc/h}$, which corresponds to the resolution of the density grid. We select this minimal smoothing scale, rather than the 2 cMpc/h previously used for the cosmic web classification, because f_{gas} only appears in the FRB DM computation, whose resolution is not limited by foreground galaxy observations and density reconstruction.

2.4 Processing the Halo Catalog

We examined whether the matter, baryons, or electrons are linked to a halo. We adopted the Caesar halo catalog provided by the official SIMBA repository. To eliminate nonphysical haloes caused by numerical artifacts, we filtered the minimum stellar mass with a threshold of $3.64 \times 10^8 h^{-1} M_\odot$, equivalent to 20 times the average mass of a gas cell. For all the feedback variants, the filtered catalogs have a maximum halo mass of about $3 \times 10^{14} h^{-1} M_\odot$. SIMBA-50, SIMBA-nox and SIMBA-nojet also have similar median halo masses ($2 \times 10^{11} h^{-1} M_\odot$) and minimum halo masses ($6 \times 10^9 h^{-1} M_\odot$). SIMBA-noagn run has a higher minimum halo mass of $1.1 \times 10^{10} h^{-1} M_\odot$, and SIMBA-nofb

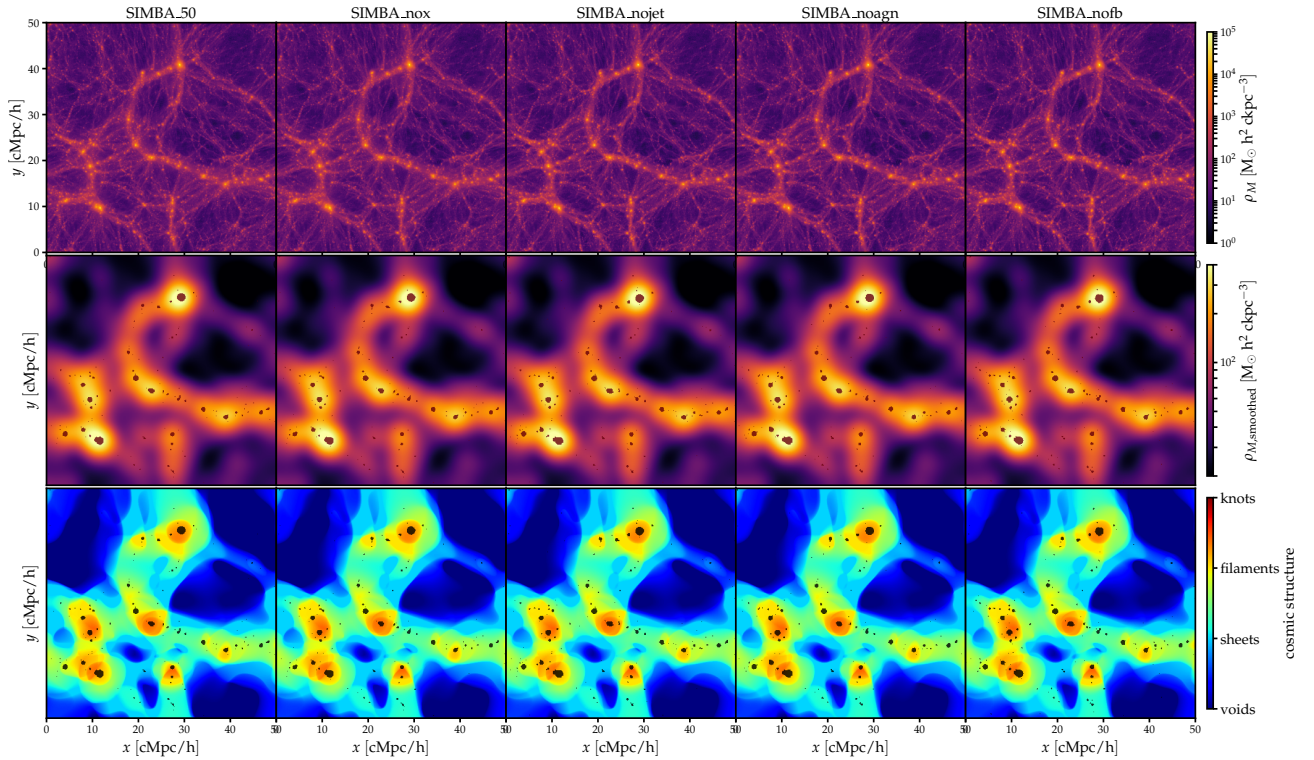


Figure 1: **Left to right:** Slices of SIMBA feedback variants (SIMBA–50, SIMBA–nox, SIMBA–nojet, SIMBA–noagn, SIMBA–nofb) with 10 cMpc/h thickness showing the full density field (dark matter and baryons) and associated cosmic web classifications. **Top row:** The slice of density field taken from the $z = 0$ snapshot. The "cosmic web" is defined with the interconnected filament and the nodes, surrounded by sheets and voids. **Middle row:** The same slice but smoothed with a Gaussian kernel with a size of 2 cMpc/h. **Right row:** corresponding averaged classification field, performed with $\lambda_{\text{th}} = 0.16$. The haloes are overplotted as masks in the middle (dark red) and right column (black). Visually, there is little change on the shape of structures among these variants.

run has a lower median halo mass of $4 \times 10^{10} h^{-1} M_{\odot}$. Utilizing the r_{200} measurements from the Caesar catalog, volumetric halo masks for each feedback variant were constructed in parallel with the cosmic web classification mask. We define the IGM as the medium beyond the r_{200} masks. These halo masks were subsequently employed for the calculation of matter distribution within the haloes and for visualization.

3 COSMIC WEB CLASSIFICATION IN FEEDBACK VARIANTS

The top panels of Figure 1 show an example $z = 0$ slice of the matter density field in the SIMBA feedback variants. Across the different feedback prescriptions, we visually find no significant differences in the full density field (top row). Given that the initial conditions are identical, the similarity of large-scale structures among the feedback variants is not surprising. At the same time, the similarity hints at the insensitivity of the large-scale density field to the feedback physics.

The matter density field smoothed with a 2 cMpc/h Gaussian kernel and the resulting cosmic web classifications are shown in the middle and bottom panels of Figure 1. The latter are also indistinguishable among the feedback variants, suggesting that the effect of feedback on the cosmic web is subtle when computed directly from the full matter density field (see also, e.g., Sunseri et al. 2023). We attribute the subtlety to the fact that the cosmic web structure at these large scales is primarily driven by gravitational interactions, which are dominated by dark matter that is largely insensitive to baryonic feedback effects.

Our smoothing with 2 cMpc/h Gaussian kernel also contributes to decreasing the apparent impact on baryonic physics. In Figure 1, we also overplot the position of dark-matter haloes on both panels. Even though the density and associated classification are similar, we note that the positions of dark-matter haloes differ slightly from one prescription to another, which may arise from the sub-Mpc impact of the feedback physics or numerical artifacts in the halo finder.

4 MATTER PARTITION IN COSMIC ENVIRONMENTS

This section illustrates the distribution of matter between the IGM and haloes under the cosmic web classification. For specific fraction numbers, refer to Appendix A.

4.1 Total mass fraction and volume fraction in the structures

The upper left panel of Figure 2 illustrates the total mass fraction, including both dark matter and baryons, within the cosmic web structures at $z = 0$. Approximately 10% of the mass is in voids, 25% in sheets, 40% in filaments, and 25% in knots. Among the various feedback mechanisms, only jet feedback slightly alters the distribution of mass across these structures. Activating jet feedback slightly decreases the mass in knots by a fraction of 0.7% while adding to the mass in sheets by a fraction of 0.6%. The results suggest the T-web classification with our choice of hyperparameters is robust against the variation of feedback models. Such robustness is anticipated since

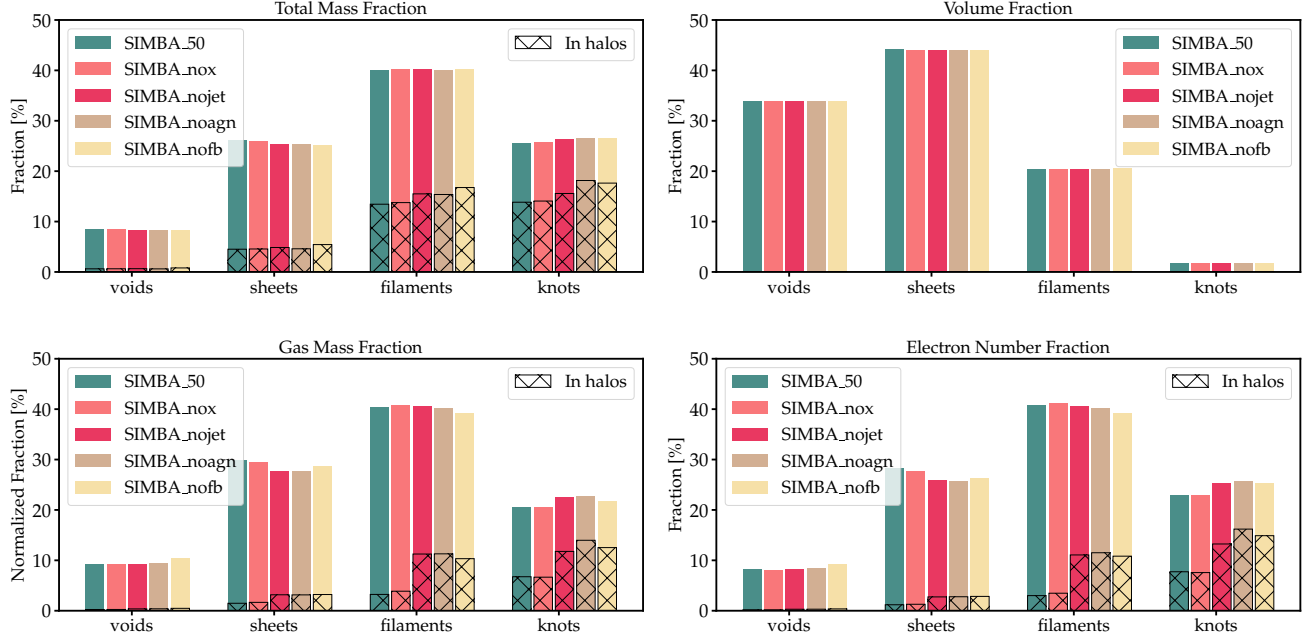


Figure 2: Fractions of total matter (dark matter and baryons, upper left), volume (upper right), gas (lower left) and free electrons (lower right) that belongs to the different large-scale structures at $z = 0$. The variation of feedback prescriptions (see Table 1) is color-coded. The fraction of matter inside haloes is shown as hatched regions, except for the volume fractions.

our classification relies on the total density field that is predominantly shaped by dark matter without feedback influences. Besides, the influence of feedback physics on baryons is likely smoothed out under the smoothing scale of 2 cMpc/h .

The panel also illustrates the fraction of matter occupied by haloes within each component of the cosmic web (hatched histograms). Across all feedback variants, we observe that a growing fraction of matter is contained within haloes as the structures become denser: approximately 40% of the matter in filaments is located in haloes, whereas in knots, this proportion increases to more than 50%. Feedback physics has a greater impact on the fraction of matter in haloes, especially in the filaments. In general, feedback prescriptions can affect halo matter fractions by a few percent. Stronger feedback results in reduced matter within haloes, as found by Khrykin et al. (2024a). This effect is primarily observed in the filaments and knots. AGN jets eject matter and prevent more efficient mass accretion in filaments and knots; stellar feedback regulates the halo accretion in filaments.

In the upper right panel of Figure 2, we show the volume fraction of cosmic web structures in the SIMBA’s feedback variants. We find that the volume fraction is highly insensitive to the sub-grid models: In all the feedback variants, the fractions of voids, sheets, filaments, and knots are 34%, 44%, 20%, and 2%, respectively. The differences between the feedback variants are within 0.1%. The insensitivity also arises from using the total mass density for cosmic web classification, which is nearly consistent across feedback variants.

4.2 Gas and free electron fraction in the structures

We further examine the distribution of baryonic matter and free electrons within the large-scale structure.

Lower left panel of Figure 2 illustrates how gas is distributed across various parts of the cosmic web, depending on feedback. The observed trend is akin to that in the total mass fraction, but

with a more pronounced effect from the feedback models: turning on jet feedback increases the gas fraction in sheets and decreases the fraction in knots by 2%. Feedback also has a subtle impact on filaments, while their gas fraction remains almost the same. Notably, removing stellar feedback increases the fraction of gas in voids and sheets while it decreases it in filaments and knots by 1%.

This can be explained by recalling that the gas fraction is mainly determined by two factors: star formation and baryon expulsion. The lack of feedback in the SIMBA–nofb run leads to more active star formation, resulting in a reduced quantity of extragalactic gas. On the other hand, AGN feedback provides enough energy to the surrounding IGM to suppress excessive star formation, but such feedback also removes the baryons from knots.

In haloes, we note a significant reduction in gas fraction due to jet feedback (as previously seen in Appleby et al. 2021; Sorini et al. 2022). This reduction is the most significant in filament haloes, with as much as a 10% decrease. AGN thermal feedback and stellar feedback also contribute to shaping the gas partition in the knots, whereas X-ray heating feedback is not as efficient. As for knots, we observe that turning off stellar feedback leads to a decrease of the gas mass fractions in haloes, due to intense star formation.

The lower right panel of Figure 2 illustrates the quantity of free electrons present within the structures. The partition of free electrons resembles the gas mass partition: jet feedback raises the free electron fraction in sheets and decreases it in knots; within haloes, jet feedback reduces the free electron fraction in knots by half, similar to the situation of gas mass fraction.

4.3 Baryon and IGM Gas Partition in different environments

One goal of this study is to enhance observational constraints on feedback mechanisms in FRB foreground mapping analysis by investigating the potential improvements to the model through the

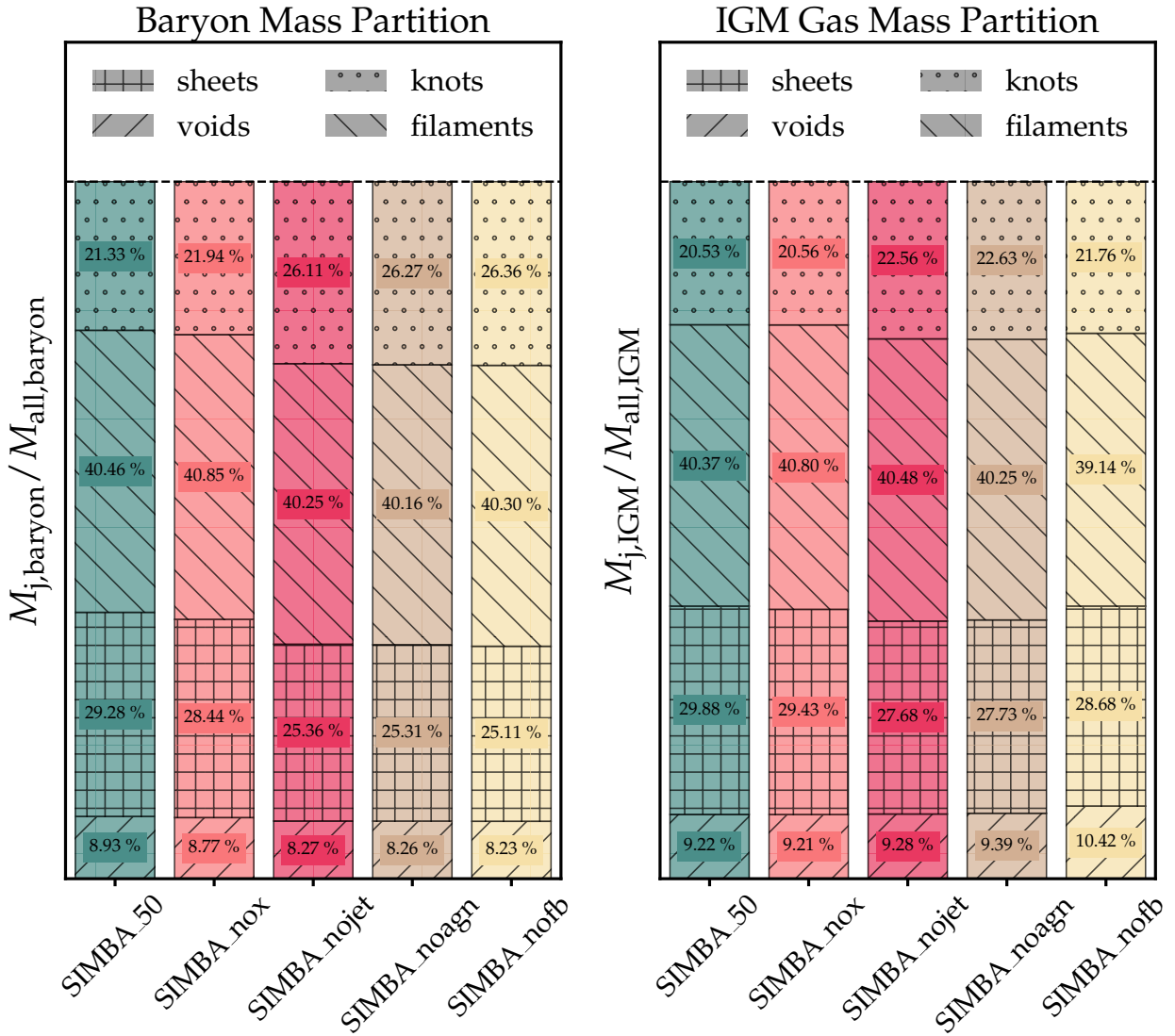


Figure 3: **Left:** the partition of baryon (gas, stars and black holes) in various structures for the different feedback models. The fractions are normalized with the baryon mass in the whole simulation box. **Right:** the partition of IGM gas (excludes haloes). The values are normalized by the total IGM gas mass in the simulation box.

integration of cosmic web information, as shown in Equation 5 and 6.

In Figure 3, we present the cosmic web partition of baryon $F_{j,\text{baryon}}$ and IGM gas $F_{j,\text{IGM}}$ with respect to different feedback physics. Importantly, in the calculation of $F_{j,\text{IGM}}$ we focus only on the IGM gas, i.e. the gas associated with haloes is excluded. Although the effect of the AGN jet feedback is very significant on the haloes, this is not automatically true for the relative matter distribution across the IGM, i.e., the distribution among voids, sheets, filaments, and knots. Indeed there is only lower than one percent effect for the baryon partition in filaments and voids from jet feedback. In contrast, knots and sheets show a few percent change, which remains minor compared to the impact of the jets on haloes. Other variations in feedback models similarly exert a negligible influence on the partitioning of IGM gas, producing differences that are less than 2%.

Our findings indicate that various feedback mechanisms account for merely slight differences (1% – 3%) in different parts of the

cosmic web normalized to either the baryon mass partition and IGM gas mass partition.

5 THE LOCAL DEPENDENCE OF IGM GAS FRACTION ON ENVIRONMENT

In Section 4 we have analyzed the distribution of IGM gas through its partition among cosmic web structures. In this section, we focus on the gas fraction in individual voxels with the goal of understanding the distribution of IGM gas inside each type of structure.

Following the definition of f_{gas} in Equation 16, we consider the correlation of the IGM gas distribution relative to the cosmic web in Section 5.1, then give a quantitative description in Section 5.2.

5.1 The correlation between f_{gas} and the Cosmic web

In Figure 4, we show the f_{gas} distribution for a 1 cMpc/h slice of SIMBA feedback variants (second row) together with the density field (first row) and the classification of the cosmic web (third row).

For SIMBA-50 and SIMBA-nox, an excess of f_{gas} is found at the outskirts of the filaments and knots, while the core regions of knots show a deficit due to jet feedback. For the other feedback variants, the variation of f_{gas} is mainly presented in the filaments; a coaxial structure of gas deficit (surrounding) and gas excess (center) forms along the visual filaments, i.e., the filaments that are clearly visually distinguishable in the matter distribution. It is worth noticing that the ‘visual’ filaments are not necessarily equivalent to the T-web filament defined in Section 2.2, mostly because of the coarse resolution scale adopted in the T-web reconstruction. The detection of the ‘visual’ filaments requires the application of filament finders using galaxy positions as tracers of the density field, such as DisPerSE (Sousbie 2011; Sousbie et al. 2011), T-Rex (Bonnaire et al. 2020), or I-DREAM (Awad et al. 2023), which is beyond the scope of this work, which requires a more volumetric method in order to unambiguously assess the IGM baryon partition.

Figure 4 shows that multiple types of physics at different scales contribute to shaping the spatial correlation. In the absence of jet feedback, the primary mechanism that influences the gas distribution is accretion. Accretion results in the aggregation of gas within high-density regions, consequently leading to a gas deficit at the outskirts of ‘visual’ filaments. In contrast, jet feedback drastically changes the correlation by ejecting gas into the IGM, creating a gas deficit within the haloes and a surplus in the surrounding filaments.

These findings bring a higher resolution perspective into our results of Section 4, where we found minimal changes in the IGM gas partition among cosmic web environments, our findings indicate that jet feedback significantly alters the distribution within the cosmic web structures. However, the impact is limited to regions near massive structures and does not extend beyond the cosmic web size (a few to ten Mpc) defined in Section 2.2.

5.2 The dependence of f_{gas} on the overdensity

Inspired by Sorini et al. (2022) and Khrykin et al. (2024a) reporting that the gas fraction f_{gas} within haloes has a dependence on the halo mass for different feedback variants, we investigate the dependence of f_{gas} on the local overdensity $\delta_m = \rho_m/\bar{\rho}_m - 1$. We show the dependence of f_{gas} on $(1 + \delta_m)$ in the leftmost panel of Figure 5. We find a similar trend to Figure 3 of Khrykin et al. (2024a). In the following, we describe the trends from high to low over-density values. For the volume with $(1 + \delta_m) \gtrsim 100$ where haloes usually reside, the f_{gas} for SIMBA-nox and SIMBA-50 shows a U-turn shape: it goes down until $\log(1 + \delta_m) \sim 2.5$, then rises again in the more massive regime. For relatively lower overdensities associated with diffuse IGM, $0.1 < (1 + \delta_m) < 10$, we find a bump with a peak $f_{\text{gas}} \sim 2$ at $(1 + \delta_m) \sim 0.3$ for these two prescriptions, due to jet feedback that ejects halo gas to the IGM and prevents accretion of IGM gas. As a result, the gas decouples with dark matter and remains in the diffuse IGM, leading to an excess of f_{gas} at $0.1 < (1 + \delta_m) < 10$. The other three feedback models, SIMBA-nofb, SIMBA-noagn and SIMBA-nojet, show a steadily decreasing relation between f_{gas} and $(1 + \delta_m)$ for high overdensity, but their f_{gas} values are always higher than the SIMBA-nox and SIMBA-50 for such large overdensities. For diffuse gas in moderate nonlinearities ($0.1 < (1 + \delta_m) < 10$) and no jet feedback, assuming the gas fraction to be at the cosmic value $f_{\text{gas}} \approx 1$ provides an unbiased approximation; For extremely

low overdensities $1 + \delta_m < 0.01$ we find all the prescriptions have $f_{\text{gas}} > 1$, which is likely due to the Gaussian smoothing operation applied to the density fields. These regions are more easily affected by the smoothing as their intrinsic density is small compared with the change introduced by the smoothing. Therefore we argue those f_{gas} values do not have a physical origin.

When taking an environment-based view, we find that the U-turn trend of f_{gas} related to the jet feedback is only present in cosmic web knots; for the other cosmic web structures, f_{gas} can be as low as zero at high overdensities. Notably, distinguishing the volume based on the cosmic web structures isolates the signal of $f_{\text{gas}} \neq 1$ in the diffuse IGM. In knots and filaments, the peak of $f_{\text{gas}} > 3$ indicates that the mean baryon content in the diffuse IGM can be three times higher than the expected value assuming gas traces the density field exactly. Within cosmic voids, however, the excess almost disappears.

We interpret the U-turn at $(1 + \delta_m) > 100$ and the bump at $0.1 < (1 + \delta_m) < 10$ as a result of strong jet feedback in the SIMBA-nox and SIMBA-50 runs. For one thing, the jet facilitates the redistribution of baryons between the IGM and haloes, with a pronounced effect within intermediate-mass haloes. In these systems, the activity of SMBHs is better fueled compared with smaller haloes, and the ejected gas has a higher probability to escape the gravitational potential well compared to that in larger haloes. Thus, the bump indicates the destination of gas expelled from haloes — they reside in the diffuse IGM, leading to the gas fraction $f_{\text{gas}} > 1$. In the absence of jet feedback, it is the star formation that dominates the variation of f_{gas} in the haloes. This results in the monotonically declining trend of f_{gas} observed in SIMBA-nojet, SIMBA-noagn, and SIMBA-50. Both stellar feedback and AGN thermal feedback still play a role in controlling star formation, which explains why the f_{gas} value is marginally higher in the SIMBA-nojet scenario. Without jets, short-range galaxy feedback in SIMBA has a minimal impact on baryon content, which leads to f_{gas} being almost one. The trend becomes stronger because the cosmic web classification filters the mass of the associated haloes, e.g. massive galaxy clusters preferentially reside in cosmic web knots.

6 DISCUSSION

In this work, we adopted the T-web method to detect the cosmic web at observationally motivated scales in SIMBA simulations with different feedback variants. Based on the classification, we investigate the impact of feedback on modifying the relative distribution of matter and gas across the cosmic web.

6.1 Comparison to previous simulation works

In this Section, we discuss our findings in the context of previous simulation works.

In Section 4.2, we find that the jet feedback has limited effect on the gas partition among the observationally motivated cosmic web environments. However, when taking a microscale view, we find that the feedback of the AGN jet influences haloes, particularly in filaments (upper left panel of Figure 2), largely due to baryon removal from haloes (lower left panel of Figure 2). In turn, the IGM gas around massive structures tends to exhibit a gas excess as the jet feedback moves halo gas to IGM (Figure 4 and 5).

The impact of jet feedback on the halo gas has been well studied in the literature. Sorini et al. (2022) found that in SIMBA, AGN jets effectively remove baryonic matter from $M_h > 10^{12} M_\odot$ haloes at redshift $z < 2$. Additionally, using the same set of simulations,

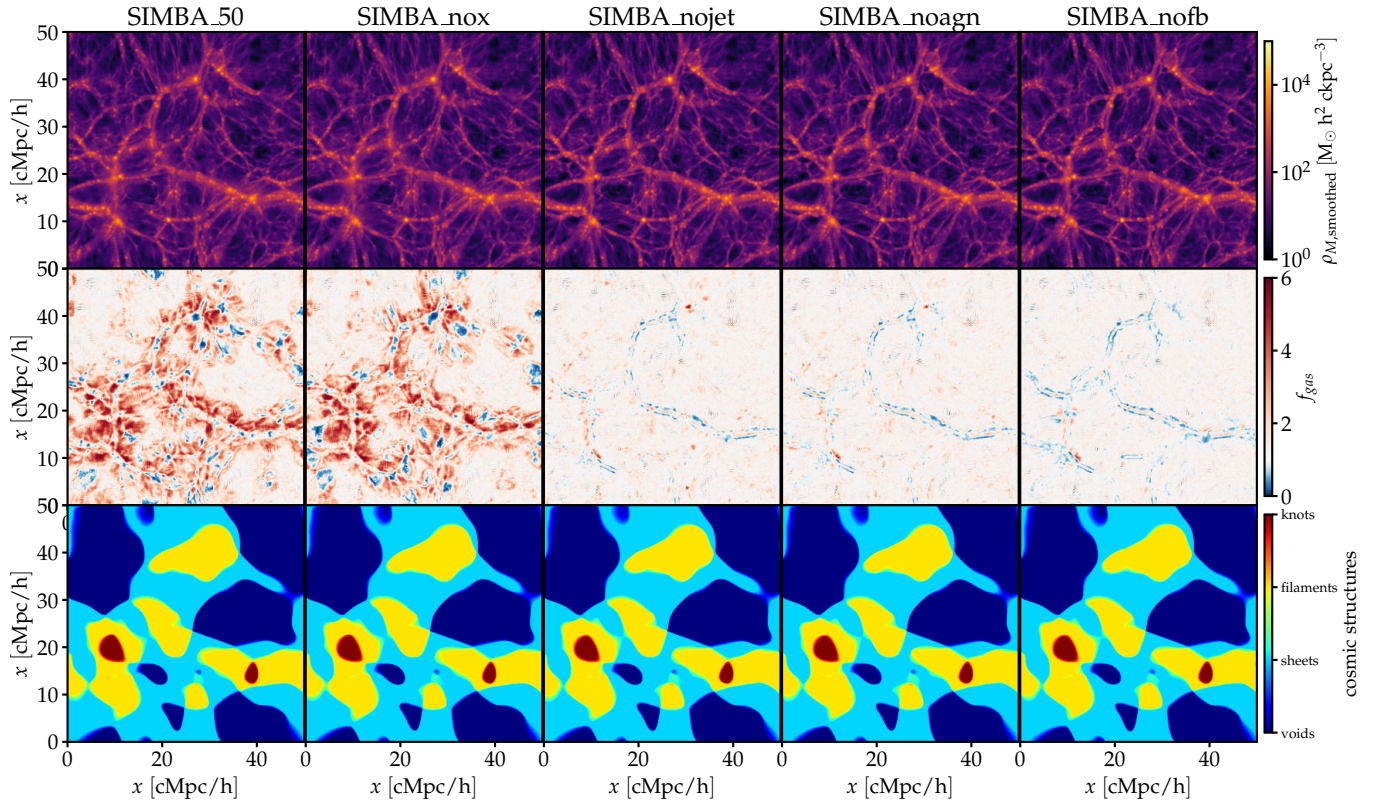


Figure 4: **Left to right:** Slices (1 cMpc/h thickness) of SIMBA feedback variants (Simba-50, Simba-nox, Simba-nojet, Simba-noagn, Simba-nofb) showing the density field, f_{gas} value and associated cosmic web classifications. **Top row:** The slice of density field taken from the $z = 0$ snapshot. **Middle row:** The f_{gas} distribution in the slices. Note the colormap is chosen to indicate relative gas deficits ($f_{\text{gas}} < 1$) as blue and gas excess ($f_{\text{gas}} > 1$) as red. **Bottom row:** Corresponding averaged classification field, performed with $\lambda_{th} = 0.16$. The calculation of f_{gas} is based on 100 ckpc/h Gaussian smoothed field in order to suppress the numerical artifacts. The deficit and excess of f_{gas} is spatially correlated with the Cosmic web classification.

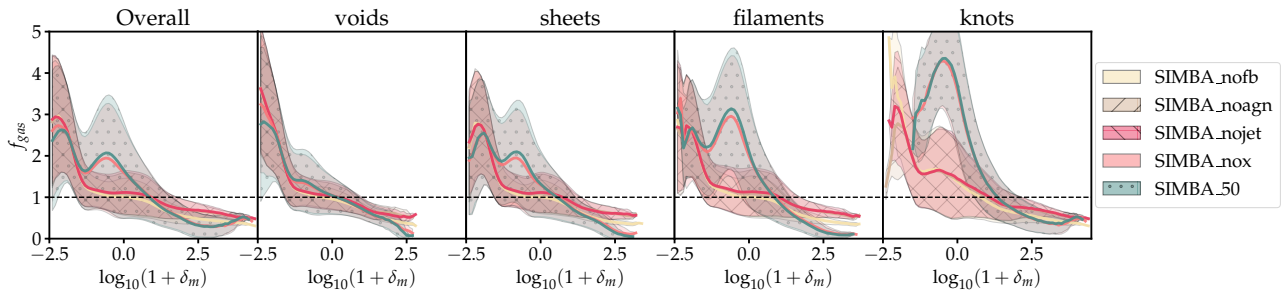


Figure 5: The gas fraction f_{gas} as a function of overdensity ($1 + \delta_m$) under 0.1 cMpc/h Gaussian smoothing, in every T-web structure and for all SIMBA feedback variants. **Left to right:** the relation in the whole simulation volume, in voids, in sheets, in filaments and in knots. The shaded regions represents 1σ range of the f_{gas} distribution. Within the SIMBA-nox and SIMBA-50 runs, we observe a U-turn pattern where $f_{\text{gas}} < 1$ (gas deficit) linked to haloes, whereas in the diffused IGM, it appears that $f_{\text{gas}} \sim 2$. The amplitude of the bump is stronger when the simulation volume is separated according to the cosmic web classification: the fraction reaches $f_{\text{gas}} > 3$ in filaments and knots. The hatched regions represent the $1-\sigma$ range of f_{gas} at a given overdensity for each feedback variant.

Khyrkin et al. (2024a) reported that AGN jets reduce the CGM mass fraction by a factor of six at $z = 0.1$ in haloes with $10^{12} M_{\odot} < M_h < 10^{14} M_{\odot}$. Our study agrees with this trend in the baryonic fraction distribution and f_{gas} for $(1 + \delta_m) > 100$. However, the influence of feedback on the relative baryon distribution across different cosmic web environments is less detectable, mainly because of the scales used in the cosmic web (which are observationally motivated).

Additionally, Sorini et al. (2022) studied the distribution of differ-

ent baryonic phases within haloes in the mass range $10^{11} - 10^{14} M_{\odot}$ in the SIMBA suite of simulations. Noting that, except for the no-feedback variant, haloes are generally baryon deficient, they showed that the halo-centric distance enclosing 90% of the cosmic baryon mass fraction varies considerably with halo mass and redshift. This scale was found to be very sensitive to the underlying feedback prescriptions and can thus be exploited as a gauge for the effectiveness of feedback at evacuating baryons from within haloes outwards. These

results were independently confirmed by Ayromlou et al. (2023), who extended the study of the dependence of the aforementioned length scale (adopting a slightly different operational definition), to the IllustrisTNG and EAGLE simulations as well. Although those recent works by Sorini et al. (2022) and Ayromlou et al. (2023) imply excess baryons around haloes as seen in Figure 4, they emphasised a halo-focused perspective motivated by X-ray and SZ observations (see also Angelinelli et al. 2022, 2023), in contrast with our study’s motivation from the FRB point of view, in which the dispersion measure is a volume-weighted probe of cosmic gas.

The work of Walker et al. (2024) aligns closely with the objectives of our study. Their research on the TNG-300 simulation categorizes cosmic structures into haloes, filaments, and voids with simple cuts on the density values and assesses their influence on FRB dispersion measures. In their findings, the filament baryon fraction decreases from approximately 90% at $z = 5$ to around 65% at $z = 0$, where the latter closely matches our ‘sheets+filaments’ baryon fraction. They also found lower DM variance for FRB sightlines in voids and suggested utilizing this for selecting FRBs that pass mainly through low-density structures to probe cosmological parameters. Our findings, illustrated in Figure 5, endorse this approach: the voids have the least feedback model dependence, which simplifies the interpretation of the DM analysis.

It should also be noted that the selection of hyperparameters can significantly affect the classification outcomes. The smoothing length R_{sm} sets the characteristic scale for cosmic web structures. This choice contributes to the uncertainty when investigating the impact of feedback on the IGM, given the scale dependence of feedback. As demonstrated in Section 3, the density fields of the SIMBA variants exhibit little visual difference, resulting in a similar cosmic web classification of the structures. In Section 4.3, we examine the impact of feedback on the matter distribution among the various cosmic web components of the IGM and report a minimal change in mass fraction, up to a few percent, which is related to our choice of observation-motivated smoothing scale, 2 cMpc/h. Ni et al. (2023) notes that the effects of the jet feedback in SIMBA gradually shrink on the scale beyond one megaparsec, whereas our structural classification, ranging from several to ten megaparsecs, is minimally influenced by this feedback.

Sunseri et al. (2023) studied the effect of baryon feedback with the TNG-300 simulation and its dark-matter-only counterpart. The authors deployed the NEXUS+ algorithm to define the cosmic web, which improved the T-web method by adopting the log-density field as input and using multiple smoothing kernels to capture the structures of different scales. The NEXUS algorithm visually suggests a multi-scale filament classification, compared to the fixed smoothing length in the T-web method used in this work with, yet the resulting mass fraction discrepancy for filaments is only 1%. The authors found that the haloes lose about 10% of their mass due to the presence of baryon feedback and a suppression of the power spectrum in massive structures. A similar trend can be found in the gas fraction shown in Figure 2, where turning on the jet feedback causes the loss of baryons in haloes.

Concerns may arise regarding the reliability of the jet model in the SIMBA simulation, considering the strong assumptions about the direction of the highly collimated jet launch. Furthermore, simulation data sets such as CAMELS (Villaescusa-Navarro et al. 2021b) suggest that SIMBA predicts the thermal evolution of the IGM gas distinctly from other cosmological simulations such as TNG and EAGLE. In fact, observations of the IGM favor the SIMBA jet feedback model in many cases. For instance Christiansen et al. (2020) and Tillman et al. (2023) find that the jet feedback in SIMBA provides

a better agreement to observations of the Ly α forest mean flux decrement and the column density distribution of absorbers, respectively, of the low redshift ($z < 1$) Lyman- α forest. The jet feedback model in SIMBA is also the most likely explanation for the ‘missing’ Lyman- α absorption around several $z \sim 2$ galaxy protoclusters as found in Dong et al. (2023); Dong et al. (2024). On the CGM scale, the results are more mixed, and comparisons with observations are less definitive. Davé et al. (2019), Robson & Davé (2020), and Jennings & Davé (2023) showed that SIMBA nicely matches X-ray observations such as the halo baryon fraction of groups, stacked X-ray luminosity vs. central galaxy K-band luminosity, and X-ray scaling relations as well as or better than many other models. However, at higher redshifts, Sorini et al. (2020) reports that the Lyman- α transmission around close quasar pairs in the SIMBA simulation does not match the observations by Prochaska et al. (2013) within a transverse separation of 150 kpc. Recently, Zhang et al. (2025) reported that SIMBA predicts well the $L_X - M_*$ (X-ray luminosity versus stellar mass) relation observed by eROSITA, and remains in broad agreement with the observation on the $L_X - M_{500c}$ (X-ray luminosity versus halo mass) relation. In contrast, (Oppenheimer et al. 2021) noted that SIMBA under-predicts central hot gas densities and over-predicts inner entropy profiles in galaxy groups. Similarly, the Gizmo-SIMBA runs from the 300 Cluster Project likewise show lower central densities than observed in clusters (Cui et al. 2022). So, SIMBA may have some issues in over-evacuating the central regions of massive haloes. Despite this, SIMBA’s highly collimated jet model does not seem unrealistic and may in fact be favored by larger-scale observations of the CGM and IGM, implying that significant gas redistribution and heating from AGN feedback is plausible.

6.2 Comparison to previous observation works

In this section, we compare our results with a few observational works.

Hussaini et al. (2025) recently examined the link between the excess of DM of FRB, denoted as $\Delta\text{DM} = \text{DM}_{\text{cosmo}} - \langle \text{DM}_{\text{cosmo}} \rangle$, and foreground large-scale structures using galaxy tracers. The study reported a weak but statistically significant correlation between DM excess and galaxy density, along with a clear DM excess for FRB sightlines with an impact parameter less than approximately 3 Mpc. These results support the hypothesis that feedback contributes to the IGM f_{gas} excess, especially near the massive structures as shown in this work.

The study conducted by Hsu et al. (2025) also reported a positive correlation between $\text{DM}_{\text{cosmic}}$ excess and galaxy number density with localised FRBs and photometric galaxy catalogs. The authors suggested that fluctuations in ionized baryons influence the dispersion measure (DM) of FRBs on a scale of several megaparsecs. Although a larger localised FRB sample and more spectroscopic follow-up are necessary to confirm this trend, it can potentially be explained by the feedback or environmental influence of f_{gas} , as demonstrated in 5. Ongoing galaxy survey programs, such as FLIM-FLAM targeted on FRB fields, or DESI (DESI Collaboration et al. 2022) and the Subaru PFS Galaxy Evolution Survey (Greene et al. 2022) on wider fields, are expected to provide a substantial dataset that facilitates the characterization of FRB sightline environments, thus playing a crucial role in validating the correlation.

6.3 Implication on FRB foreground mapping as a feedback probe

As mentioned in Section 4, galaxy feedback of any form only causes percent-level relative changes in the IGM gas partitioning across the different components of the cosmic web at the scale of 2 cMpc/h. Although the partition between the halo CGM gas and broader IGM has been shown to be sensitive to galaxy feedback prescriptions (Khrykin et al. 2024a), there appears to be limited additional information from considering the gas fractions between different cosmic web components (as in Equation 5 and 6) at the scales we can actually reconstruct the web in observations, especially in current generations of FRB survey FLIMFLAM (Lee et al. 2022; Khrykin et al. 2024b).

Nevertheless, it is meaningful to define an environment-dependent (or density-dependent) f_{gas} to allow for a more precise DM_{IGM} estimation. In FLIMFLAM, the contribution of the IGM gas to DM_{IGM} is modeled as a quantity linearly tracing the distribution of the matter density field (Equation 3). In other words, we show in Section 5 that the assumption $\rho_{\text{gas,IGM}} = (1 + \delta_m)\bar{\rho}_{\text{gas,IGM}}$ (required by Equation 3) may not hold when jet feedback is present, such as in the SIMBA-50 and SIMBA-nojet simulations. This long-range collimated jet feedback is likely to raise f_{gas} in low-density regions relative to high-density ones. Overall, this could lead to a bimodal variation in the DM_{IGM} estimation, introducing systematics to the FRB analysis.

To account for the influence of jet feedback on DM_{IGM} , we suggest employing a local gas fraction f_{gas} dependent on overdensity, rather than global f_{IGM} . Figure 5 shows the f_{gas} distribution by overdensity; this correction may serve as a bias term when translating $(1 + \delta_m)$ into the density of electron numbers.

At the current spatial resolution of the density reconstructions in the FLIMFLAM survey (around 2 cMpc/h), the changes to f_{gas} seem to minimally affect the DM budget across the cosmic web. Borrow et al. (2020) reports that the 90% baryons in SIMBA simulations with jets are spread within 3 cMpc/h around their initial Lagrangian regions (the comoving volume in the initial condition that corresponds to the halo volume at lower redshifts), extensive yet smaller than the structures defined here. Meanwhile, the typical spread of the no-jet runs is merely 1 cMpc/h, comparable to the largest haloes in the simulation. The findings affirm the use of full-density-based reconstruction treatment in FLIMFLAM, with the separation of the halo CGM and large-scale IGM as a probe of galaxy feedback. Given the reconstructed cell size of approximately 2 cMpc, modeling large-scale baryonic effects as secondary is justified. Nonetheless, the deviation of gas fraction from unity becomes more significant when analyzing structures below the megaparsec scale. In the upcoming FLIMFLAM data release, we will evaluate an improved density reconstruction method (Dong et al. in prep), potentially highlighting the impact of non-unity f_{gas} for diffused IGM gas.

7 CONCLUSION

In this study, we use the cosmic web classification based on eigenvalues (T-web) to examine the distribution of IGM gas in SIMBA with special consideration on the influence of feedback mechanisms. The key findings are as follows.

- On scales of the reconstructed cosmic web (typically \gtrsim a few Mpc), the classification of large-scale environments via the T-web method remains largely stable against variations in feedback models. Changes in these feedback models induce only minor variations in classification outcomes (see Figure 1). Furthermore, the associated mass and volume fractions indicate that the classification

is relatively insensitive to feedback physics (see the upper panels of Figure 2).

- Analysis of the gas (lower left panel of Figure 2) and electron distribution (lower right panel of Figure 2) indicates that jet feedback is crucial in modifying their distribution, although in a relatively subtle way. More baryons remain in sheets and less accrete onto knots when jet feedback is active. Jet feedback also effectively removes baryons from the haloes, as confirmed by Khrykin et al. (2024a) and Sorini et al. (2022).
- Jet feedback minimally affects ($\lesssim 1\%$) the partition of the IGM gas across the cosmic web structures (Figure 3). This indicates a limited advantage in incorporating differential baryon fractions across cosmic web structures for the FRB foreground mapping analysis (in Equation 5 and 6).
- By extending the definition of gas fraction f_{gas} from individual haloes in Khrykin et al. (2024a) to voxels with 0.1 cMpc/h size, We note that variations in the f_{gas} values are spatially correlated with physical large-scale structures, especially when jet feedback is involved (Figure 4). Analysis of the dependence of f_{gas} on the overdensity field suggests that jet feedback causes an excess baryon ratio in the diffuse IGM for $0.1 < 1 + \delta_m < 10$ (Figure 5), mainly from the volume of filament or knots.

Our results highlight the role of AGN jet feedback in shaping the baryon distribution within haloes and the IGM, as revealed by the SIMBA simulation and analyzed through the cosmic web.

We test the extension of the FLIMFLAM baryonic model with cosmic web classification, and report the dependence of f_{gas} on the local IGM overdensity, which is a notable systematic to be addressed with future FRB foreground mapping projects. Alternatively, modification of f_{gas} might be achieved through a baryon painting neural network (e.g., Troster et al. 2019; Horowitz et al. 2022; Chadayammuri et al. 2023; Williams et al. 2023). The relationship could be represented using emulators trained in cosmological simulation datasets for machine learning uses, such as CAMELS (Villaescusa-Navarro et al. 2021b; Guo & Lee 2025), and incorporated into the FRB foreground mapping data model (see Villaescusa-Navarro et al. 2021a; Mohammad et al. 2022 for associated machine learning applications).

Although our primary motivation stems from FRB foreground mapping, the broader implications extend to general FRB-based constraints on the cosmic baryon budget. Looking ahead, forthcoming radio surveys such as CHIME, DSA-2000, and CRAFT, combined with deep optical follow-ups from Subaru/PFS, DESI, Roman, and LSST, will enable a powerful synergy between radio transients and traditional galaxy surveys. This multiwavelength approach promises to significantly advance our understanding of the baryon distribution in the low-redshift universe.

ACKNOWLEDGEMENTS

Kavli IPMU is supported by the World Premier International Research Center Initiative (WPI), MEXT, Japan. This work was performed in part at the Center for Data-Driven Discovery, Kavli IPMU (WPI). This study was supported by the Forefront Physics and Mathematics Program to Drive Transformation (FoPM), a World-leading Innovative Graduate Study (WINGS) Program, the University of Tokyo. CD thanks Sunil Simha and Ilya Khrykin for useful discussions. FD would like to thank Kavli IPMU for having allowed this collaboration, and especially the *idark* team, which has been providing a quality service that was very valuable for the smooth running of this project.

DATA AVAILABILITY

The SIMBA cosmological simulation is publicly available at [Simba project repository](#). The data products in this work, including the density field and cosmic web classification, will be shared upon request to the authors.

REFERENCES

- Angelinelli M., Ettori S., Dolag K., Vazza F., Ragagnin A., 2022, *A&A*, **663**, L6
- Angelinelli M., Ettori S., Dolag K., Vazza F., Ragagnin A., 2023, *A&A*, **675**, A188
- Anglés-Alcázar D., Faucher-Giguère C.-A., Quataert E., Hopkins P. F., Feldmann R., Torrey P., Wetzel A., Kereš D., 2017, *Monthly Notices of the Royal Astronomical Society: Letters*, **472**, L109–L114
- Appleby S., Davé R., Sorini D., Storey-Fisher K., Smith B., 2021, *MNRAS*, **507**, 2383
- Appleby S., Davé R., Sorini D., Cui W., Christiansen J., 2023, *MNRAS*, **519**, 5514
- Ata M., Kitaura F.-S., Müller V., 2015, *MNRAS*, **446**, 4250
- Ata M., et al., 2017, *MNRAS*, **467**, 3993
- Awad P., et al., 2023, *MNRAS*, **520**, 4517
- Ayromlou M., Nelson D., Pillepich A., 2023, *MNRAS*, **524**, 5391
- Barišić I., et al., 2017, *The Astrophysical Journal*, **847**, 72
- Batten A. J., Duffy A. R., Flynn C., Gupta V., Ryan-Weber E., Wijers N., 2022, *MNRAS*, **512**, L49
- Best P. N., Heckman T. M., 2012, *Monthly Notices of the Royal Astronomical Society*, **421**, 1569–1582
- Bondi H., 1952, *Monthly Notices of the Royal Astronomical Society*, **112**, 195
- Bonnaire T., Aghanim N., Decelle A., Douspis M., 2020, *A&A*, **637**, A18
- Borrow J., Anglés-Alcázar D., Davé R., 2020, *MNRAS*, **491**, 6102
- Bradley L., Davé R., Cui W., Smith B., Sorini D., 2022, *arXiv e-prints*, p. [arXiv:2203.15055](#)
- Bregman J. N., 2007, *ARA&A*, **45**, 221
- Bryan G. L., et al., 2014, *ApJS*, **211**, 19
- CHIME/FRB Collaboration et al., 2021, *ApJS*, **257**, 59
- Cautun M., van de Weygaert R., Jones B. J. T., Frenk C. S., 2014, *MNRAS*, **441**, 2923
- Cen R., Fang T., 2006, *ApJ*, **650**, 573
- Cen R., Ostriker J. P., 1999, *ApJ*, **514**, 1
- Cen R., Ostriker J. P., 2006, *ApJ*, **650**, 560
- Cen R., Tripp T. M., Ostriker J. P., Jenkins E. B., 2001, *ApJ*, **559**, L5
- Chadayammuri U., Ntampaka M., Zuhone J., Bogdán Á., Kraft R. P., 2023, *MNRAS*, **526**, 2812
- Chiu I., et al., 2018, *MNRAS*, **478**, 3072
- Choi E., Ostriker J. P., Naab T., Johansson P. H., 2012, *The Astrophysical Journal*, **754**, 125
- Christiansen J. F., Davé R., Sorini D., Anglés-Alcázar D., 2020, *MNRAS*, **499**, 2617
- Cooke R., 2024, *arXiv e-prints*, p. [arXiv:2409.06015](#)
- Cordes J. M., Chatterjee S., 2019, *ARA&A*, **57**, 417
- Cui W., et al., 2022, *MNRAS*, **514**, 977
- DESI Collaboration et al., 2022, *AJ*, **164**, 207
- Davé R., et al., 2001, *ApJ*, **552**, 473
- Davé R., Oppenheimer B. D., Katz N., Kollmeier J. A., Weinberg D. H., 2010, *MNRAS*, **408**, 2051
- Davies J. J., Crain R. A., McCarthy I. G., Oppenheimer B. D., Schaye J., Schaller M., McAlpine S., 2019, *MNRAS*, **485**, 3783
- Davies J. J., Crain R. A., Oppenheimer B. D., Schaye J., 2020, *MNRAS*, **491**, 4462
- Davé R., Thompson R., Hopkins P. F., 2016, *Monthly Notices of the Royal Astronomical Society*, **462**, 3265–3284
- Davé R., Anglés-Alcázar D., Narayanan D., Li Q., Rafieferantsoa M. H., Appleby S., 2019, *Monthly Notices of the Royal Astronomical Society*, **486**, 2827–2849
- Dong C., Lee K.-G., Ata M., Horowitz B., Momose R., 2023, *ApJ*, **945**, L28
- Dong C., Lee K.-G., Davé R., Cui W., Sorini D., 2024, The Effect of AGN Feedback on the Lyman-alpha Forest Signature of Galaxy Protoclusters at $z \approx 2.3$ ([arXiv:2402.13568](#))
- Fang T., Marshall H. L., Lee J. C., Davis D. S., Canizares C. R., 2002, *ApJ*, **572**, L127
- Ferraro S., Hill J. C., Battaglia N., Liu J., Spergel D. N., 2016, *Phys. Rev. D*, **94**, 123526
- Forero-Romero J. E., Hoffman Y., Gottlöber S., Klypin A., Yepes G., 2009, *Monthly Notices of the Royal Astronomical Society*, **396**, 1815–1824
- Fukugita M., Peebles P. J. E., 2004, *ApJ*, **616**, 643
- Fukugita M., Hogan C. J., Peebles P. J. E., 1998, *ApJ*, **503**, 518
- Glowacki M., Lee K.-G., 2024, *arXiv e-prints*, p. [arXiv:2410.24072](#)
- Greene J., Bezanson R., Ouchi M., Silverman J., the PFS Galaxy Evolution Working Group 2022, *arXiv e-prints*, p. [arXiv:2206.14908](#)
- Guo Q., Lee K.-G., 2025, *arXiv e-prints*, p. [arXiv:2501.16709](#)
- Haardt F., Madau P., 2012, *The Astrophysical Journal*, **746**, 125
- Hahn O., Porciani C., Carollo C. M., Dekel A., 2007, *Monthly Notices of the Royal Astronomical Society*, **375**, 489–499
- Haider M., Steinhauser D., Vogelsberger M., Genel S., Springel V., Torrey P., Hernquist L., 2016, *MNRAS*, **457**, 3024
- Hallman E. J., O’Shea B. W., Burns J. O., Norman M. L., Harkness R., Wagner R., 2007, *ApJ*, **671**, 27
- Heckman T. M., Best P. N., 2014, *Annual Review of Astronomy and Astrophysics*, **52**, 589–660
- Heckman T. M., Thompson T. A., 2017, *arXiv e-prints*, p. [arXiv:1701.09062](#)
- Hong S. E., Ryu D., Kang H., Cen R., 2014, *ApJ*, **785**, 133
- Hopkins P. F., Quataert E., 2011, *Monthly Notices of the Royal Astronomical Society*, **415**, 1027–1050
- Hopkins P. F., Kereš D., Oñorbe J., Faucher-Giguère C.-A., Quataert E., Murray N., Bullock J. S., 2014, *MNRAS*, **445**, 581
- Horowitz B., Dornfest M., Lukić Z., Harrington P., 2022, *ApJ*, **941**, 42
- Hsu T.-Y., et al., 2025, *arXiv e-prints*, p. [arXiv:2505.03326](#)
- Huang Y., et al., 2024, *arXiv e-prints*, p. [arXiv:2408.12864](#)
- Hussaini M., Connor L., Konietzka R. M., Ravi V., Faber J., Sharma K., Sherman M., 2025, *arXiv e-prints*, p. [arXiv:2506.04186](#)
- Iwamoto K., Brachwitz F., Nomoto K., Kishimoto N., Umeda H., Hix W. R., Thielemann F., 1999, *The Astrophysical Journal Supplement Series*, **125**, 439–462
- Jennings F., Davé R., 2023, *MNRAS*, **526**, 1367
- Kang H., Ryu D., Cen R., Song D., 2005, *ApJ*, **620**, 21
- Kang H., Ryu D., Cen R., Ostriker J. P., 2007, *ApJ*, **669**, 729
- Kennicutt Jr. R. C., 1998, *The Astrophysical Journal*, **498**, 541–552
- Khrykin I. S., Sorini D., Lee K.-G., Davé R., 2024a, *MNRAS*, **529**, 537
- Khrykin I. S., et al., 2024b, *ApJ*, **973**, 151
- Kocz J., et al., 2019, *MNRAS*, **489**, 919
- Kovács O. E., Bogdán Á., Smith R. K., Kraft R. P., Forman W. R., 2019, *ApJ*, **872**, 83
- Kravtsov A. V., Klypin A., Hoffman Y., 2002, *ApJ*, **571**, 563
- Krumholz M. R., Gnedin N. Y., 2011, *The Astrophysical Journal*, **729**, 36
- Lee K.-G., Ata M., Khrykin I. S., Huang Y., Prochaska J. X., Cooke J., Zhang J., Batten A., 2022, *The Astrophysical Journal*, **928**, 9
- Lim S. H., Barnes D., Vogelsberger M., Mo H. J., Nelson D., Pillepich A., Dolag K., Marinacci F., 2021, *MNRAS*, **504**, 5131
- Macquart J.-P., et al., 2010, *Publ. Astron. Soc. Australia*, **27**, 272
- Macquart J. P., et al., 2020, *Nature*, **581**, 391
- Martizzi D., et al., 2019, *Monthly Notices of the Royal Astronomical Society*, **486**, 3766–3787
- McCarthy I. G., Schaye J., Bird S., Le Brun A. M. C., 2017, *MNRAS*, **465**, 2936
- Mohammad F. G., Villaescusa-Navarro F., Genel S., Anglés-Alcázar D., Vogelsberger M., 2022, *ApJ*, **941**, 132
- Muratov A. L., Kereš D., Faucher-Giguère C.-A., Hopkins P. F., Quataert E., Murray N., 2015, *Monthly Notices of the Royal Astronomical Society*, **454**, 2691–2713
- Neeleman M., Prochaska J. X., Ribaud J., Lehner N., Howk J. C., Rafelski M., Kanekar N., 2016, *ApJ*, **818**, 113
- Ni Y., et al., 2023, *ApJ*, **959**, 136

- Nicastro F., et al., 2018, *Nature*, **558**, 406
- Nomoto K., Tominaga N., Umeda H., Kobayashi C., Maeda K., 2006, *Nuclear Physics A*, **777**, 424–458
- Oppenheimer B. D., Davé R., 2006, *Monthly Notices of the Royal Astronomical Society*, **373**, 1265–1292
- Oppenheimer B. D., Davé R., Katz N., Kollmeier J. A., Weinberg D. H., 2012, *MNRAS*, **420**, 829
- Oppenheimer B. D., Babul A., Bahé Y., Butsky I. S., McCarthy I. G., 2021, *Universe*, **7**, 209
- Perna M., Lanzuisi G., Brusa M., Mignoli M., Cresci G., 2017a, *Astronomy and Astrophysics*, **603**, A99
- Perna M., Lanzuisi G., Brusa M., Cresci G., Mignoli M., 2017b, *Astronomy and Astrophysics*, **606**, A96
- Pillepich A., et al., 2018, *MNRAS*, **473**, 4077
- Planck Collaboration et al., 2016, *A&A*, **594**, A13
- Planck Collaboration et al., 2020, *A&A*, **641**, A6
- Platts E., Weltman A., Walters A., Tendulkar S. P., Gordin J. E. B., Kandhai S., 2019, *Phys. Rep.*, **821**, 1
- Prochaska J. X., et al., 2013, *ApJ*, **776**, 136
- Prochaska J. X., et al., 2017, *ApJ*, **837**, 169
- Rahmati A., Pawlik A. H., Raičević M., Schaye J., 2013, *Monthly Notices of the Royal Astronomical Society*, **430**, 2427–2445
- Robson D., Davé R., 2020, *MNRAS*, **498**, 3061
- Röttgers B., Naab T., Cernetic M., Davé R., Kauffmann G., Borthakur S., Foidl H., 2020, *MNRAS*, **496**, 152
- Sanidas S., Caleb M., Driessen L., Morello V., Rajwade K., Stappers B. W., 2018, in *Weltvrede P., Perera B. B. P., Preston L. L., Sanidas S.*, eds, IAU Symposium Vol. 337, *Pulsar Astrophysics the Next Fifty Years*. pp 406–407, doi:10.1017/S1743921317009310
- Schaye J., et al., 2010, *MNRAS*, **402**, 1536
- Schaye J., et al., 2015, *MNRAS*, **446**, 521
- Schmidt M., 1959, *ApJ*, **129**, 243
- Shao J., Zhang P., Lin W., Jing Y., Pan J., 2011, *MNRAS*, **413**, 628
- Simha S., et al., 2020, *ApJ*, **901**, 134
- Smith B. D., et al., 2016, *Monthly Notices of the Royal Astronomical Society*, **466**, 2217–2234
- Sorini D., Davé R., Anglés-Alcázar D., 2020, *MNRAS*, **499**, 2760
- Sorini D., et al., 2022, *Monthly Notices of the Royal Astronomical Society*, **516**, 883
- Sorini D., Bose S., Davé R., Anglés-Alcázar D., 2024, *The Open Journal of Astrophysics*, **7**, 115
- Sousbie T., 2011, *MNRAS*, **414**, 350
- Sousbie T., Pichon C., Kawahara H., 2011, *MNRAS*, **414**, 384
- Steigman G., 2010, *arXiv e-prints*, p. arXiv:1008.4765
- Stocke J. T., Keeney B. A., Danforth C. W., Shull J. M., Froning C. S., Green J. C., Penton S. V., Savage B. D., 2013, *ApJ*, **763**, 148
- Sunseri J., Li Z., Liu J., 2023, *Phys. Rev. D*, **107**, 023514
- Tillman M. T., Burkhart B., Tonnesen S., Bird S., Bryan G. L., Anglés-Alcázar D., Davé R., Genel S., 2023, *apjl*, **945**, L17
- Tollet É., Cattaneo A., Macciò A. V., Dutton A. A., Kang X., 2019, *MNRAS*, **485**, 2511
- Tornatore L., Borgani S., Viel M., Springel V., 2010, *MNRAS*, **402**, 1911
- Troster T., Ferguson C., Harnois-Déraps J., McCarthy I. G., 2019, *MNRAS*, **487**, L24
- Villaescusa-Navarro F., et al., 2021a, *arXiv e-prints*, p. arXiv:2109.10360
- Villaescusa-Navarro F., et al., 2021b, *ApJ*, **915**, 71
- Vogelsberger M., et al., 2014, *MNRAS*, **444**, 1518
- Walker C. R. H., Spitler L. G., Ma Y.-Z., Cheng C., Artale M. C., Hummels C. B., 2024, *A&A*, **683**, A71
- Williams I. M., Khan A., McQuinn M., 2023, *MNRAS*, **520**, 3626
- Yoshikawa K., Yamasaki N. Y., Suto Y., Ohashi T., Mitsuda K., Tawara Y., Furuzawa A., 2003, *PASJ*, **55**, 879
- Zhang Y., et al., 2025, *A&A*, **693**, A197
- de Graaff A., Cai Y.-C., Heymans C., Peacock J. A., 2019, *A&A*, **624**, A48

APPENDIX A: DATA TABLE

In this appendix, we show the fraction data (Table A1) used in Figure 2 and 3.

APPENDIX B: CONVERGENCE TEST

We report the mass and volume fraction when varying the mass resolution or box size of the simulation in Table B1. SIMBA-100 and SIMBA-25 runs are introduced to test the impact of the box size. Both runs are equipped with full feedback physics and shares the same mass resolution with the SIMBA-50 run. Their box sizes are 100 cMpc/h and 25 cMpc/h, respectively. Comparing SIMBA-100 with SIMBA-50, we find the difference in either mass and volume fraction between this run and the SIMBA-50 run is within 2%. For the SIMBA-25, the difference in fractions is up to 5%. This result is acceptable given the smaller box would suffer severer cosmic variance. The SIMBA-hi run constitutes a high-resolution simulation, characterized by a 8× mass resolution in comparison to SIMBA-50, within a box size of 25 cMpc/h. A notable distinction is observed in the statistical properties of sheets and filaments. Specifically, the mass fraction of sheets diminished by 3%, while the volume fraction of sheets decreased by 5%. Meanwhile, the mass fraction of filaments augmented by 5%, with their volume fraction increasing by 3%.

The choice of λ_{th} for the T-web classification is evaluated in Table B2. Fraction values from $\lambda_{\text{th}} = 0.05$ to $\lambda_{\text{th}} = 0.40$ indicate that the variations in mass fractions are +14%, +4%, -13%, -5% for voids, sheets, filaments, and knots, respectively. The volume fraction demonstrates greater sensitivity to the selection of λ_{th} , especially for the voids: the volume fraction of voids increases by approximately 25% from $\lambda_{\text{th}} = 0.05$ to $\lambda_{\text{th}} = 0.40$.

Total Mass Fraction [%]	voids	sheets	filaments	knots
SIMBA-50	8.39(11.46)	26.10(31.99)	39.99(39.42)	25.52(17.14)
SIMBA-nox	8.37(11.51)	25.90(31.91)	40.14(39.52)	25.60(17.06)
SIMBA-nojet	8.26(11.94)	25.33(32.34)	40.10(38.96)	26.31(16.76)
SIMBA-noagn	8.25(12.41)	25.28(33.79)	40.04(40.40)	26.43(13.40)
SIMBA-nofb	8.23(12.52)	25.12(33.16)	40.13(39.36)	26.51(14.96)
Volume Fraction [%]	voids	sheets	filaments	knots
SIMBA-50	33.90(33.95)	44.06(44.11)	20.28(20.25)	1.76(1.69)
SIMBA-nox	33.90(33.95)	44.02(44.07)	20.32(20.29)	1.76(1.69)
SIMBA-nojet	33.85(33.91)	43.98(44.04)	20.41(20.36)	1.77(1.70)
SIMBA-noagn	33.84(33.89)	43.98(44.04)	20.41(20.38)	1.77(1.69)
SIMBA-nofb	33.80(33.86)	43.96(44.02)	20.47(20.43)	1.78(1.69)
Gas Fraction [%]	voids	sheets	filaments	knots
SIMBA-50	9.22(10.17)	29.88(32.21)	40.37(42.06)	20.53(15.56)
SIMBA-nox	9.21(10.23)	29.43(31.76)	40.80(42.20)	20.56(15.82)
SIMBA-nojet	9.28(12.10)	27.68(33.41)	40.48(39.88)	22.56(14.61)
SIMBA-noagn	9.39(12.62)	27.73(34.55)	40.25(40.74)	22.63(12.09)
SIMBA-nofb	10.42(13.54)	28.68(34.67)	39.14(39.23)	21.76(12.56)
Electron Number Fraction [%]	voids	sheets	filaments	knots
SIMBA-50	8.20(9.12)	28.27(30.85)	40.68(42.87)	22.84(17.16)
SIMBA-nox	8.09(9.04)	27.72(30.24)	41.27(43.20)	22.93(17.52)
SIMBA-nojet	8.25(10.93)	25.81(31.78)	40.61(40.71)	25.33(16.58)
SIMBA-noagn	8.44(11.74)	25.74(33.21)	40.16(41.44)	25.65(13.62)
SIMBA-nofb	9.25(12.50)	26.20(32.85)	39.24(39.98)	25.32(14.67)

Table A1: The fraction of total mass (dark matter and baryon), volume, baryonic gas and electron number in SIMBA feedback variants according to cosmic web classification. Note values inside parentheses are statistics with haloes excluded.

Total Mass Fraction [%]	voids	sheets	filaments	knots
SIMBA-100	8.12	28.29	40.45	23.15
SIMBA-25	7.09	29.23	42.61	21.06
SIMBA-hi	8.72	23.77	45.20	22.31
Volume Fraction [%]	voids	sheets	filaments	knots
SIMBA-100	32.05	46.74	19.86	1.35
SIMBA-25	29.70	48.03	20.22	2.04
SIMBA-hi	36.04	38.63	23.46	1.87

Table B1: The fraction of total mass and volume in box size and mass resolution variants.

Total Mass Fraction [%]	voids	sheets	filaments	knots
$(\lambda_{\text{th}}, R_{\text{sm}}) = (0.05, 2 \text{ cMpc/h})$	4.27	23.89	44.59	27.25
$(\lambda_{\text{th}}, R_{\text{sm}}) = (0.10, 2 \text{ cMpc/h})$	6.00	25.15	42.50	26.34
$(\lambda_{\text{th}}, R_{\text{sm}}) = (0.15, 2 \text{ cMpc/h})$	8.01	25.93	40.41	25.65
$(\lambda_{\text{th}}, R_{\text{sm}}) = (0.20, 2 \text{ cMpc/h})$	9.99	26.66	38.35	25.00
$(\lambda_{\text{th}}, R_{\text{sm}}) = (0.25, 2 \text{ cMpc/h})$	11.93	27.49	36.29	24.28
$(\lambda_{\text{th}}, R_{\text{sm}}) = (0.30, 2 \text{ cMpc/h})$	14.06	27.66	34.74	23.53
$(\lambda_{\text{th}}, R_{\text{sm}}) = (0.35, 2 \text{ cMpc/h})$	15.92	28.05	33.12	22.90
$(\lambda_{\text{th}}, R_{\text{sm}}) = (0.40, 2 \text{ cMpc/h})$	17.73	28.42	31.73	22.12
Volume Fraction [%]	voids	sheets	filaments	knots
$(\lambda_{\text{th}}, R_{\text{sm}}) = (0.05, 2 \text{ cMpc/h})$	20.94	50.04	26.81	2.22
$(\lambda_{\text{th}}, R_{\text{sm}}) = (0.10, 2 \text{ cMpc/h})$	26.87	47.64	23.50	1.99
$(\lambda_{\text{th}}, R_{\text{sm}}) = (0.15, 2 \text{ cMpc/h})$	32.75	44.68	20.77	1.80
$(\lambda_{\text{th}}, R_{\text{sm}}) = (0.20, 2 \text{ cMpc/h})$	38.35	41.52	18.50	1.63
$(\lambda_{\text{th}}, R_{\text{sm}}) = (0.25, 2 \text{ cMpc/h})$	43.47	38.48	16.57	1.48
$(\lambda_{\text{th}}, R_{\text{sm}}) = (0.30, 2 \text{ cMpc/h})$	47.91	35.84	14.91	1.34
$(\lambda_{\text{th}}, R_{\text{sm}}) = (0.35, 2 \text{ cMpc/h})$	51.67	33.63	13.48	1.22
$(\lambda_{\text{th}}, R_{\text{sm}}) = (0.40, 2 \text{ cMpc/h})$	55.01	31.61	12.27	1.10

Table B2: The fraction of total mass and volume in λ_{th} variants.